arXiv:1405.6522v1 [cond-mat.str-el] 26 May 2014

Crystal field splitting in $Sr_{n+1}Ir_nO_{3n+1}$ ($n = 1, 2$) iridates probed by x-ray Raman spectroscopy

M. Moretti Sala,[1,*] M. Rossi,[1] A. Al-Zein,[1] S. Boseggia,[2,3] E. C. Hunter,[4] R. S. Perry,[2] D. Prabhakaran,[5] A. T. Boothroyd,[5] N. B. Brookes,[1] D. F. McMorrow,[2] G. Monaco,[6] and M. Krisch[1]

[1] *European Synchrotron Radiation Facility, CS 40220, 38043 Grenoble Cedex 9, France*
[2] *London Centre for Nanotechnology and Department of Physics and Astronomy, University College London, London WC1E 6BT, United Kingdom*
[3] *Diamond Light Source Ltd, Diamond House, Harwell Science and Innovation Campus, Didcot, Oxfordshire OX11 0DE, United Kingdom*
[4] *School of Physics and Astronomy, The University of Edinburgh, Mayfield Road, Edinburgh EH9 2TT, United Kingdom*
[5] *Clarendon Laboratory, Department of Physics, University of Oxford, Parks Road, Oxford OX1 3PU, United Kingdom*
[6] *Dipartimento di Fisica, Università di Trento, via Sommarive 14, 38123 Povo (TN), Italy*

Non-resonant Raman spectroscopy in the hard X-ray regime has been used to explore the electronic structure of the first two members of the Ruddlesden-Popper series $Sr_{n+1}Ir_nO_{3n+1}$ of iridates. By tuning the photon energy transfer around 530 eV we have been able to explore the oxygen K near edge structure with bulk sensitivity. The angular dependence of the spectra has been exploited to assign features in the 528-535 eV energy range to specific transitions involving the Ir $5d$ orbitals. This has allowed us to extract reliable values for both the t_{2g}–e_g splitting arising from the cubic component of the crystal field ($10Dq$), in addition to the splitting of the e_g orbitals due to tetragonal distortions. The values we obtain are (3.8, 1.6) eV and (3.55, 1.9) eV for Sr_2IrO_4 and $Sr_3Ir_2O_7$, respectively.

I. INTRODUCTION

$5d$ transition metal oxides have recently attracted considerable interest as they display unusual properties primarily resulting from the effect of large spin-orbit coupling[1–8]. Of particular interest is the electronic nature of Sr_2IrO_4[9] and $Sr_3Ir_2O_7$[10]: despite the large $5d$ bandwidth and weak correlation, both of which favour a metallic character, these systems are insulators. The opening of an electronic gap has been explained by means of a Hubbard-like model, in which the effect of correlation is enhanced by the strong spin-orbit coupling which narrows the effective $5d$ bandwidth isolating the so-called $j_{\rm eff} = 1/2$ state[1,3]. The $j_{\rm eff} = 1/2$ state results from a particular hierarchy of energies at play, most especially the crystal field and the spin-orbit coupling.

Sr_2IrO_4 ($Sr_3Ir_2O_7$) is the $n = 1$ ($n = 2$) member of the Ruddlesden-Popper series, $Sr_{n+1}Ir_nO_{3n+1}$, and is built by the stacking of IrO_2 (bi-)layers, in which IrO_6 octahedra share the corner oxygens. The dominant perturbation to the half-filled $5d$ iridium states in these compounds comes from the cubic component of the crystal field, written conventionally as $10Dq$. Indeed the t_{2g}–e_g splitting, of order several eV, is often considered to be large enough that the e_g states can be neglected, allowing the basic electronic structure to be understood in terms of a single hole occupying the t_{2g} orbitals (tetravalent iridium is $5d^5$). In order to describe properly the ground state wave function of this hole, spin-orbit coupling and residual crystal-field effects with symmetry lower than cubic, such as tetragonal in the post-perovskite $CaIrO_3$[11,12] or trigonal in pyrochlore $R_2Ir_2O_7$ (R = rare earth element)[13], need to be considered. At the single-ion level, this is achieved by diagonalizing the Hamiltonian $\mathcal{H} = \zeta \mathbf{L}\cdot\mathbf{S} - \Delta L_z^2$ in the t_{2g} orbitals basis-set[12–16], where ζ is the spin-orbit coupling and Δ is the tetragonal (trigonal) crystal-field splitting.

Strictly speaking, the $j_{\rm eff} = 1/2$ ground state is realized only for $\Delta = 0$, i.e. for a perfectly cubic symmetry. In real materials this condition is relaxed to $|\Delta| \ll \zeta$. Estimates of Δ in Sr_2IrO_4 ($\Delta = -0.01$ eV[17]) and its sister compound Ba_2IrO_4($\Delta = 0.05$ eV[18]) indeed confirm that the requirement on the relative magnitude of $|\Delta|$ and ζ is realized, since the spin-orbit coupling in these materials of order $\sim$0.5 eV[1,18,19]. One has to keep in mind, however, that the scenario of the $j_{\rm eff} = 1/2$ ground state holds true only when the e_g states do not contribute to the ground state wave function, i.e. if the cubic component of the crystal field $10Dq$ is much larger than the spin-orbit coupling, $10Dq \gg \zeta$. Indeed, the contribution of the e_g states has been invoked as a possible cause of the departure of $CaIrO_3$ from the pure $j_{\rm eff} = 1/2$ ground state in LDA+SO+U calculations[20].

Theoretical estimates of $10Dq$ in Sr_2IrO_4 range from 1.8[21] to 5 eV[22]. Experimentally, various x-ray techniques have been used to estimate $10Dq$, including x-ray absorption spectroscopy (XAS), resonant elastic (REXS) and inelastic (RIXS) x-ray scattering. For example, soft XAS at the O K edge has been used to probe the empty iridium $5d$ states through hybridization with the oxygen $2p$ orbitals[1,18], providing values of $10Dq$ for Sr_2IrO_4[23] and $Sr_3Ir_2O_7$[24] in the range 2.5 eV to 4 eV. However, this particular technique is highly surface sensitive, especially when performed in total-electron-yield (TEY) mode, which compromises the reliability of the extracted value of $10Dq$. The possibility that surface and bulk

properties might be different in iridium oxides was highlighted by Liu *et al.*, who reported the existence of weak metallicity in the near-surface electronic structure of $Sr_3Ir_2O_7$ while its bulk is known to be insulating[25]. In addition to the surface sensitivity, one has to deal with self-absorption effects in total-fluorescence-yield (TFY) detected XAS. As self-absorption is dependent on photon energy and experimental geometry, extreme caution has to be taken when corrections to the spectra are applied. XAS at the Ir $L_{2,3}$ edges ensures bulk-sensitivity, but self-absorption equally affects hard XAS in TFY mode. Moreover, it suffers from the sizeable broadening of features due to the $2p$ core-hole lifetime which obscures details of the electronic structure close to the Fermi energy. This problem can at least be overcome to a certain degree by measuring partial-fluorescence-yield (PFY) detected XAS[26]: this technique provides very similar information to that of conventional XAS, but with the advantage that a shallower core-hole is left in the final state of the decay process selected by energy-discriminating the photons emitted due to radiative decay. For example, in the case of the $L\alpha_1$ ($L\alpha_2$) emission line of iridium, if Γ_{2p} is the lifetime broadening of the $2p_{3/2}$ core-hole, and Γ_{3d} is that of the $3d_{5/2}$ ($3d_{3/2}$) core-hole, then the PFY broadening will be given by $1/\sqrt{1/\Gamma_{2p}^2 + 1/\Gamma_{3d}^2} \approx \Gamma_{3d}$, since $\Gamma_{3d} \ll \Gamma_{2p}$. However, even if the benefits of PFY XAS are evident, it is still difficult to extract quantitative information on $10Dq$ from such measurements[27,28].

Resonant x-ray magnetic scattering (RXMS)[3,6,17,29] and resonant inelastic x-ray scattering (RIXS)[15,30–32] in the hard x-ray regime also provide rough estimates of the cubic component of the crystal field from the RXMS/RIXS energy dependence. Indeed, that the intensity of both magnetic reflections in RXMS and intra-t_{2g} excitations in RIXS are enhanced a few eV below the main absorption line has been interpreted as a signature of the t_{2g}–e_g splitting. Again, however, both of these techniques suffer from self-absorption effects due to the proximity of the scattered photon energy to the Ir $L_{2,3}$ absorption edges.

The present work was designed to provide a reliable, bulk-sensitive probe of the electronic structure of iridium oxides. We therefore used non-resonant inelastic x-ray scattering (NIXS) in the hard x-ray energy range, more specifically x-ray Raman spectroscopy (XRS), to probe the bulk properties of iridium oxides. XRS is a x-ray scattering technique in which the energy of the incoming and scattered photons is far from absorption edges of the material, making XRS a self-absorption-free and bulk-sensitive probe[33]. Indeed, the XRS cross-section in the limit of small momentum transfer $|\mathbf{q}|$ (i.e. in the dipole limit) is formally identical to that of XAS, with $\mathbf{q}$ playing the role of photon polarization: the XRS cross-sections is then proportional to $|\langle f|\mathbf{q}\cdot\mathbf{r}|i\rangle|^2$, where $|i\rangle$ and $|f\rangle$ are the many-body electronic wave functions of the initial and final state of the system, respectively[33]. The main drawback of this technique is the low count-rate, which is partially overcome by collecting the scattered photons over a large solid angle. In the following we show that XRS allows the precise determination of the cubic component of the crystal-field splitting in the compounds Sr_2IrO_4 and $Sr_3Ir_2O_7$, thus offering an alternative spectroscopic tool for the investigation of the electronic structure of iridium oxides.

II. EXPERIMENTAL DETAILS

X-ray Raman spectroscopy measurements were performed at the ID20 beam line of the European Synchrotron Radiation Facility (ESRF), Grenoble. The X-rays produced by four U26 undulators were monochromatized to an energy-resolution of $\Delta E_{\rm i} \simeq 0.3$ eV by the simultaneous use of a Si(111) high heat-load liquid-nitrogen cooled monochromator and a Si(311) post-monochromator. The x-rays were then focused at the sample position by means of a Kirkpatrick-Baez mirror system down to a spot size of 10×20 μm^2 (vertical $\times$ horizontal, FWHM). The scattered X-rays were collected by 12 crystal-analyzers exploiting the Si(660) reflection close to backscattering geometry (at a fixed Bragg angle of 88.5°, corresponding to $E_{\rm o} = 9670$ eV) and detected by a Maxipix detector[34] with pixel size of 55×55 μm^2. The resulting energy resolution was $\Delta E \simeq 0.7$ eV. In order to obtain the XRS spectrum, the incident photon energy $E_{\rm i}$ was varied in the energy range from $E_{\rm i} - E_{\rm o} = 0$ (the elastic energy) to $E_{\rm i} - E_{\rm o} = 570$ eV, thus covering the oxygen K edge. The accumulation time/spectrum was about 2 hours and several spectra were recorded to improve the counting statistics. XRS spectra were collected in two different scattering geometries, corresponding to the momentum transfer $\mathbf{q}$ along the sample c-axis and in the ab-plane, respectively. In both geometries, the scattering plane was vertical and the incident X-rays linearly polarized in the horizontal plane. XAS spectra were recorded at the ID08 beam line of the ESRF in the TFY mode.

Single crystals of Sr_2IrO_4 and $Sr_3Ir_2O_7$, with dimensions of $\sim 0.5 \times 0.5 \times 0.2$ mm^3, were were grown using the flux method described in Ref. 35. All spectra were recorded at room temperature.

III. RESULTS AND DISCUSSION

Figure 1 shows XRS scans for Sr_2IrO_4 (a) and $Sr_3Ir_2O_7$ (b) across the oxygen K edge for $\mathbf{q} \parallel (001)$ (black) and $\mathbf{q} \parallel (100)$ (red dots). The scattering angle was fixed to $2\theta = 60°$, corresponding to a momentum transfer of $|\mathbf{q}| \simeq 6$ Å^{-1}. The background was removed by subtracting a linear fit to the pre-edge region at energies lower than 528 eV. The spectra were then normalized to unit area. For both samples, spectra taken in the two geometries are distinctly different, revealing a very strong orientation dependence of the XRS signal. In particular, one notes

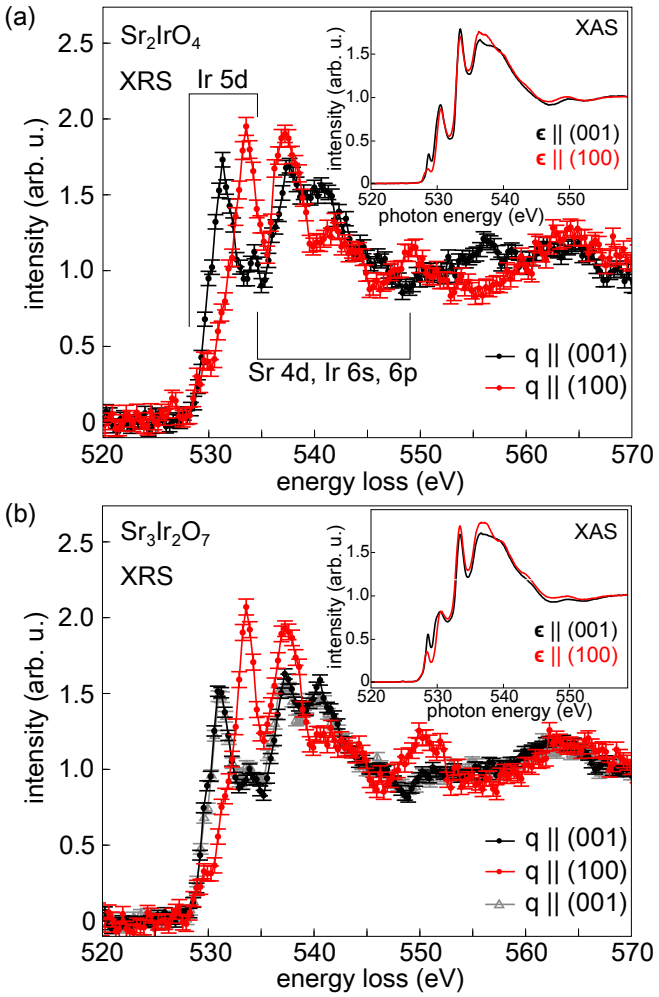


Figure 1. XRS spectra of (a) Sr_2IrO_4 and (b) $Sr_3Ir_2O_7$ for transferred momenta $\mathbf{q} \parallel (001)$ (black) and $\mathbf{q} \parallel (100)$ (red dots) with $|\mathbf{q}| \simeq 6$ Å^{-1} (scattering angle $2\theta = 60°$). Gray triangles in (b) represent the XRS spectrum of $Sr_3Ir_2O_7$ with $|\mathbf{q}| \simeq 10$ Å^{-1} (scattering angle $2\theta = 120°$). XAS spectra at the O K edge of the two compounds for incoming polarization $\boldsymbol{\epsilon} \parallel (001)$ (black) and $\boldsymbol{\epsilon} \parallel (100)$ (red line) are also shown in the insets.

a large change of spectral weight between the two main features in the 530-535 eV energy range.

In agreement with XAS results[23,36,37], the 528-535 eV energy region is dominated by transitions to the Ir $5d$ states through the hybridization with O $2p$ orbitals, while higher energy features correspond to excitations involving Ir $6s$, $6p$ and Sr $4d$ states[38], as indicated in Fig. 1. For comparison, TFY XAS spectra were measured on the very same samples. These are shown in the insets of Fig. 1. Continuous black and red lines correspond to orthogonal directions of the photon polarization, $\boldsymbol{\epsilon} \parallel (001)$ and $\boldsymbol{\epsilon} \parallel (100)$, respectively. As expected, the overall shape is similar to that of the XRS spectra, but the dichroic effect in the XAS spectra is very small, in stark contrast to the strong orientation dependence of the XRS measurements performed on the same samples. In order to rule out any contribution higher than dipolar to the XRS spectra, we investigated the $|\mathbf{q}|$ dependence of the XRS cross-section in $Sr_3Ir_2O_7$: by setting $2\theta = 120°$, corresponding to $|\mathbf{q}| \simeq 10$ Å^{-1} (gray triangles in Fig. 1(b)), we note that the overall shape of the spectrum perfectly matches with that acquired for $|\mathbf{q}| \simeq 6$ Å^{-1}, thus implying that the momentum dependence of the XRS is negligible. We therefore attribute the discrepancy between XRS and XAS measurements to potential surface and/or self-absorption effects affecting soft x-ray techniques. This observation underlines the importance of complementing surface-sensitive techniques with bulk-sensitive probes.

In order to analyse our data we have calculated the number of peaks expected in the 530-535 eV energy interval and their corresponding spectral weights by pursuing the analogy between the XRS and XAS cross-sections. The relevant transitions are those from O $1s$ to $2p$ states with the latter hybridised with the Ir $5d$ orbitals[1,18,24]. The hybridization strength is calculated according to the orbital overlap model[39] with the hopping integral $t_{pd\mu}$ written as

$$t_{pd\mu} = V_{pd\mu} r^{-\alpha}, \qquad (1)$$

where $V_{pd\mu}$ is a constant depending on the bond type (μ=π or σ), r is the Ir-O distance ($r_A = 2.06$ Å and $r_P = 1.98$ Å for apical and in-plane oxygens, respectively, in Sr_2IrO_4[9]; while $r_A = 2.02$ Å and $r_P = 1.99$ Å in $Sr_3Ir_2O_7$[40]) and $\alpha = 3.5$[41]. It should be noted that $V_{pd\sigma}$ and $V_{pd\pi}$ are related by $V_{pd\pi} = -V_{pd\sigma}/\sqrt{3}$[41].

Since the hybridization strength is inversely proportional to the distance between the atoms involved, we can distinguish the contributions of the apical (A) and in-plane (P) oxygens. Let us consider the apical oxygens first: the O $2p_z$ state hybridizes with the Ir $5d$ $3z^2 - r^2$ states, while the $2p_x$ ($2p_y$) mixes with the zx (yz) orbitals. For the in-plane oxygens, $2p_z$ hybridizes with the yz and zx orbitals, while $2p_x$ and $2p_y$ are mixed with the xy, $3z^2 - r^2$ and $x^2 - y^2$ orbitals. This is summarized in Fig. 2.

It remains to consider the cross-sections associated with transitions to different orbitals. In the framework of a single-ion model, these are obtained by calculating the matrix elements corresponding to the dipolar $1s \rightarrow 2p_i$ transitions ($i = x, y, z$)[18]. The cross-section is proportional to the product of $|t_{pd\mu}|^2$, n the number of available final $5d$ states and a polarisation factor. The polarization (transferred momentum) dependence of the XAS (XRS, in the dipole limit) cross-sections to the $2p_x$, $2p_y$ and $2p_z$ states are given by $\sin^2\theta\cos^2\varphi$, $\sin^2\theta\sin^2\varphi$ and $\cos^2\theta$, respectively, where θ and φ are the Eulerian angles describing the direction of $\boldsymbol{\epsilon}$ ($\mathbf{q}$) in the sample reference system, as sketched in Fig. 2. Merging the cross-section angular dependence and the hybridization between Ir $5d$-O $2p$ states, we obtain the polarization (transferred momentum) dependence of the transitions to the xy, yz, zx, $3z^2 - r^2$, $x^2 - y^2$ orbitals as reported in Table I. Note that we have used $n_{xy} = n_{yz} = n_{zx} = 1/3$

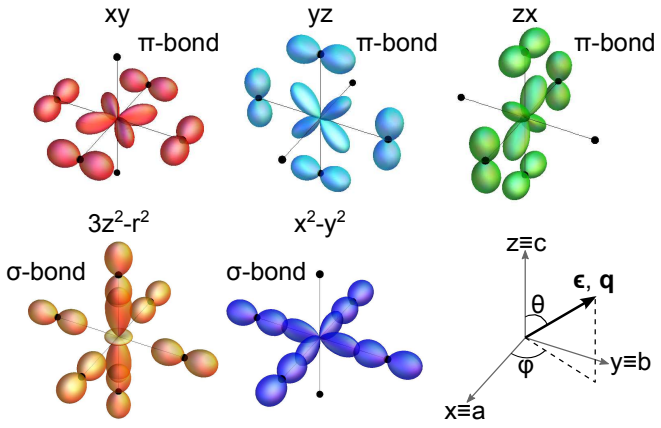


Figure 2. Sketch of the symmetry of the t_{2g} (top) and e_g (bottom) orbitals involved in the O $2p$-Ir $5d$ hybridization. The Eulerian angles θ and φ describing the direction of $\boldsymbol{\epsilon}$ or $\mathbf{q}$ in the sample reference system are also shown.

Table I. Polarization dependence of the O $1s \rightarrow$ O $2p$-Ir $5d$ dipolar transitions.

	Apical O	In-plane O
xy	0	$2V_{pd\pi}^2 n_{\mathrm{xy}} r_{\mathrm{P}}^{-2\alpha} \sin^2\theta$
yz	$2V_{pd\pi}^2 n_{\mathrm{yz}} r_{\mathrm{A}}^{-2\alpha} \sin^2\theta \sin^2\varphi$	$2V_{pd\pi}^2 n_{\mathrm{yz}} r_{\mathrm{P}}^{-2\alpha} \cos^2\theta$
zx	$2V_{pd\pi}^2 n_{\mathrm{yz}} r_{\mathrm{A}}^{-2\alpha} \sin^2\theta \cos^2\varphi$	$2V_{pd\pi}^2 n_{\mathrm{yz}} r_{\mathrm{P}}^{-2\alpha} \cos^2\theta$
$3z^2-r^2$	$2V_{pd\sigma}^2 n_{3z^2-r^2} r_{\mathrm{A}}^{-2\alpha} \cos^2\theta$	$V_{pd\sigma}^2 n_{3z^2-r^2} r_{\mathrm{P}}^{-2\alpha} \sin^2\theta$
x^2-y^2	0	$\sqrt{3}V_{pd\sigma}^2 n_{x^2-y^2} r_{\mathrm{P}}^{-2\alpha} \sin^2\theta$

and $n_{3z^2-r^2} = n_{x^2-y^2} = 2$ expected for the $j_{\mathrm{eff}} = 1/2$ state.

For the specific geometries used in our experiments, it transpires that only two transitions are allowed when $\mathbf{q} \parallel (001)$ ($\theta = 0$) and four when $\mathbf{q} \parallel (100)$ ($\theta = 90°$ and $\varphi = 0$). The appropriate cross-sections are given in Table II. We therefore performed a fitting of our model to the data by adjusting the number of peaks accordingly and constraining their relative spectral weight to the calculated one. Extra peaks were introduced in the fit to mimic the high energy features: one for $\mathbf{q} \parallel (100)$ and two for $\mathbf{q} \parallel (001)$, respectively. The result of the fitting is shown in Fig. 3 for Sr_2IrO_4 and in Fig. 4 for $Sr_3Ir_2O_7$. We emphasise that, apart from an overall scale factor for the amplitude, the energy position and full width at half maximum (FWHM) of the curves are the only free fitting parameters: their values are summarized in Table II. The agreement between the fit and the experimental data is remarkably good in both scattering geometries, allowing us to unambiguously assign each feature. In particular, the intense features at 531.4 (531.2) and 534.0 (533.7) eV in Sr_2IrO_4 ($Sr_3Ir_2O_7$) correspond to excitations to the $3z^2-r^2$ and x^2-y^2 orbitals via the apical and in-plane oxygens, respectively. This peak assignment is consistent with the work of Moon *et al.* on Sr_2IrO_4[23], Schmidt *et al.* on Sr_2RuO_4[37] and Park *et al.* on $Sr_3Ir_2O_7$[24].

We are now in a position to extract the cubic component of the crystal field $10Dq$. This is given by the energy difference between the centres of mass of the e_g and t_{2g} states for in-plane oxygens. In view of the small tetragonal crystal field measured in Sr_2IrO_4 ($|\Delta| = 0.01$ eV[17]), we consider the splitting of the t_{2g} states due to spin-orbit coupling only in the calculation of $10Dq$. We obtain 3.80 ± 0.82 eV in Sr_2IrO_4 and 3.55 ± 0.13 eV in $Sr_3Ir_2O_7$, assuming $\zeta \simeq 0.4$ eV[1]. Estimates of $10Dq$ extracted from XAS and RXMS/RIXS measurements are consistent with our results. The cubic component of the crystal field is thus very large compared to the other energy scales of the system, namely the spin orbit coupling and the tetragonal crystal field, therefore validating the initial hypothesis that $10Dq$ is the dominant energy scale. Finally, in addition to the estimate of the cubic component

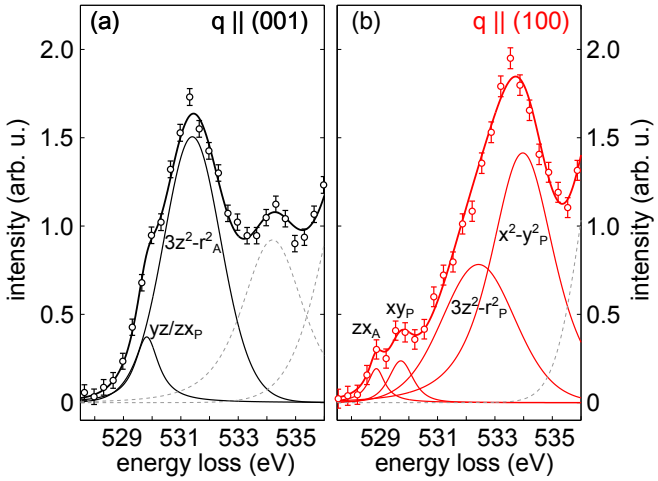


Figure 3. Experimental (open dots) and constrained fit to the XRS spectra (solid thick line) of Sr_2IrO_4 for (a) $\mathbf{q} \parallel (001)$ and (b) $\mathbf{q} \parallel (100)$. The fitting curves are plotted in solid lines, while the extra-peaks are reported in dashed gray lines.

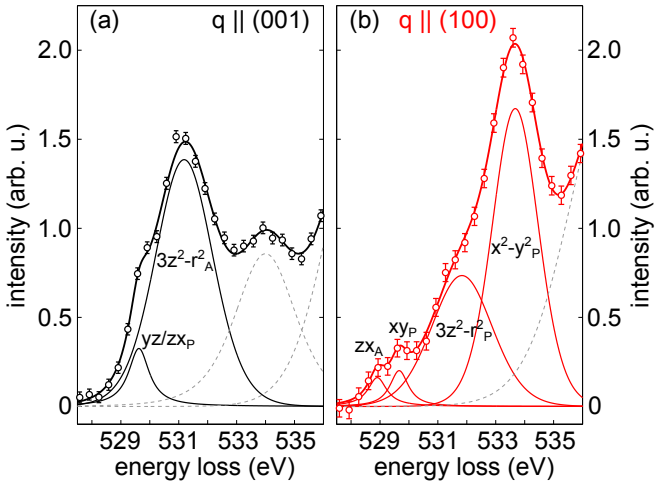


Figure 4. Experimental (open dots) and constrained fit to the XRS spectra (solid thick line) of $Sr_3Ir_2O_7$ for (a) $\mathbf{q} \parallel (001)$ and (b) $\mathbf{q} \parallel (100)$. The fitting curves are plotted in solid lines, while the extra-peaks are reported in dashed gray lines.

Table II. Cross-sections, fitted energy positions and FWHM of electronic dipolar transitions in Sr_2IrO_4 and $Sr_3Ir_2O_7$.

	$\mathbf{q} \parallel (001)$	$\mathbf{q} \parallel (100)$	Energy loss (eV) Sr_2IrO_4	FWHM (eV) Sr_2IrO_4	Energy loss (eV) $Sr_3Ir_2O_7$	FWHM (eV) $Sr_3Ir_2O_7$
$xy/yz/zx_A$		$2V^2_{pd\pi} n_{yz} r_A^{-2\alpha}$	528.9 ± 0.11	0.71 ± 0.35	528.9 ± 0.10	0.78 ± 0.30
$xy/yz/zx_P$	$4V^2_{pd\pi} n_{yz} r_P^{-2\alpha}$	$2V^2_{pd\pi} n_{xy} r_P^{-2\alpha}$	529.8 ± 0.05	1.0 ± 0.17	529.6 ± 0.03	0.87 ± 0.10
$3z^2 - r_A^2$	$2V^2_{pd\sigma} n_{3z^2-r^2} r_A^{-2\alpha}$		531.4 ± 0.05	2.4 ± 0.18	531.2 ± 0.05	2.4 ± 0.15
$3z^2 - r_P^2$		$V^2_{pd\sigma} n_{3z^2-r^2} r_P^{-2\alpha}$	532.4 ± 0.75	3.0 ± 0.67	531.8 ± 0.12	2.5 ± 0.26
$x^2 - y_A^2$						
$x^2 - y_P^2$		$\sqrt{3} V^2_{pd\sigma} n_{x^2-y^2} r_P^{-2\alpha}$	534.0 ± 0.35	2.6 ± 0.46	533.7 ± 0.05	1.9 ± 0.06

of the crystal field, we can deduce the sign of the tetragonal contribution to the crystal field from the splitting of the e_g states (1.6 ± 0.82 eV in Sr_2IrO_4 and by 1.9 ± 0.13 eV in $Sr_3Ir_2O_7$). Indeed, the fact that the $x^2 - y^2$ orbital is the highest in energy is consistent with structural studies indicating an elongation of the IrO_6 cage in both compounds. Note that, for tetragonally distorted octahedra, the description of d states requires two parameters, Ds and Dt, in addition to the main crystal-field parameter $10Dq$. The splitting of e_g and t_{2g} states is then given by $4Ds + 5Dt$ and $3Ds - 5Dt$ ($= \Delta$), respectively[42]. In the absence of spin-orbit coupling, the t_{2g} states are almost degenerate ($\Delta \approx 0$), implying $3Ds \approx 5Dt$. A finite splitting of the e_g states is therefore compatible with the realization of the $j_{\rm eff} = 1/2$ ground state in Sr_2IrO_4 and $Sr_3Ir_2O_7$.

IV. CONCLUSIONS

By exploiting the orientation dependence of oxygen K edge XRS cross-sections in Sr_2IrO_4 and $Sr_3Ir_2O_7$, we have been able to assign spectral features in the 528-535 eV energy range to specific transitions involving the Ir $5d$ orbitals. These assignments allow us to extract the value of the cubic crystal-field splitting $10Dq$ of 3.80 ± 0.82 and 3.55 ± 0.13 eV in Sr_2IrO_4 and $Sr_3Ir_2O_7$, respectively. In addition, the tetragonal crystal field was found to split the e_g states by 1.6 ± 0.82 eV in Sr_2IrO_4 and by 1.9 ± 0.13 eV in $Sr_3Ir_2O_7$. It is important to stress that the reliability of these values of the crystal field splittings obtained in our study is enhanced by the bulk sensitivity of the XRS technique.

V. ACKNOWLEDGMENTS

The authors are grateful for technical support by C. Henriquet and R. Verbeni, and all the colleagues from the ESRF support groups.

* marco.moretti@esrf.fr

[1] B. J. Kim, H. Jin, S. J. Moon, J.-Y. Kim, B.-G. Park, C. S. Leem, J. Yu, T. W. Noh, C. Kim, S.-J. Oh, J.-H. Park, V. Durairaj, G. Cao, and E. Rotenberg, Phys. Rev. Lett. **101**, 076402 (2008).

[2] S. J. Moon, H. Jin, K. W. Kim, W. S. Choi, Y. S. Lee, J. Yu, G. Cao, A. Sumi, H. Funakubo, C. Bernhard, and T. W. Noh, Phys. Rev. Lett. **101**, 226402 (2008).

[3] B. J. Kim, H. Ohsumi, T. Komesu, S. Sakai, T. Morita, H. Takagi, and T. Arima, Science **323**, 1329 (2009).

[4] D. Pesin and L. Balents, Nat. Phys. **6**, 376 (2010).

[5] F. Wang and T. Senthil, Phys. Rev. Lett. **106**, 136402 (2011).

[6] J. W. Kim, Y. Choi, J. Kim, J. F. Mitchell, G. Jackeli, M. Daghofer, J. van den Brink, G. Khaliullin, and B. J. Kim, Phys. Rev. Lett. **109**, 037204 (2012).

[7] H. Watanabe, T. Shirakawa, and S. Yunoki, Phys. Rev. Lett. **110**, 027002 (2013).

[8] W. Witczak-Krempa, G. Chen, Y. B. Kim, and L. Balents, Annual Review of Condensed Matter Physics **5**, 57 (2014).

[9] M. K. Crawford, M. A. Subramanian, R. L. Harlow, J. A. Fernandez-Baca, Z. R. Wang, and D. C. Johnston, Phys. Rev. B **49**, 9198 (1994).

[10] G. Cao, Y. Xin, C. S. Alexander, J. E. Crow, P. Schlottmann, M. K. Crawford, R. L. Harlow, and W. Marshall, Phys. Rev. B **66**, 214412 (2002).

[11] S. Hirai, M. D. Welch, F. Aguado, and S. A. T. Redfern, Z. Kristallogr. **224**, 345 (2009).

[12] K. Ohgushi, J.-i. Yamaura, H. Ohsumi, K. Sugimoto, S. Takeshita, A. Tokuda, H. Takagi, M. Takata, and T.-h. Arima, Phys. Rev. Lett. **110**, 217212 (2013).

[13] L. Hozoi, H. Gretarsson, J. P. Clancy, B.-G. Jeon, B. Lee, K. H. Kim, V. Yushankhai, P. Fulde, D. Casa, T. Gog, J. Kim, A. H. Said, M. H. Upton, Y.-J. Kim, and J. van den Brink, Phys. Rev. B **89**, 115111 (2014).

[14] L. J. P. Ament, G. Khaliullin, and J. van den Brink, Phys. Rev. B **84**, 020403 (2011).

[15] X. Liu, V. M. Katukuri, L. Hozoi, W.-G. Yin, M. P. M. Dean, M. H. Upton, J. Kim, D. Casa, A. Said, T. Gog, T. F. Qi, G. Cao, A. M. Tsvelik, J. van den Brink, and

J. P. Hill, Phys. Rev. Lett. **109**, 157401 (2012).
[16] M. Moretti Sala, S. Boseggia, D. F. McMorrow, and G. Monaco, Phys. Rev. Lett. **112**, 026403 (2014).
[17] S. Boseggia, H. C. Walker, J. Vale, R. Springell, Z. Feng, R. S. Perry, M. M. Sala, H. M. Rønnow, S. P. Collins, and D. F. McMorrow, Journal of Physics: Condensed Matter **25**, 422202 (2013).
[18] M. Moretti Sala, M. Rossi, S. Boseggia, J. Akimitsu, N. B. Brookes, M. Isobe, M. Minola, H. Okabe, H. M. Rønnow, L. Simonelli, D. F. McMorrow, and G. Monaco, Phys. Rev. B **89**, 121101 (2014).
[19] S. Boseggia, R. Springell, H. C. Walker, H. M. Rønnow, C. Rüegg, H. Okabe, M. Isobe, R. S. Perry, S. P. Collins, and D. F. McMorrow, Phys. Rev. Lett. **110**, 117207 (2013).
[20] A. Subedi, Phys. Rev. B **85**, 020408 (2012).
[21] D. Haskel, G. Fabbris, M. Zhernenkov, P. P. Kong, C. Q. Jin, G. Cao, and M. van Veenendaal, Phys. Rev. Lett. **109**, 027204 (2012).
[22] H. Jin, H. Jeong, T. Ozaki, and J. Yu, Phys. Rev. B **80**, 075112 (2009).
[23] S. J. Moon, M. W. Kim, K. W. Kim, Y. S. Lee, J.-Y. Kim, J.-H. Park, B. J. Kim, S.-J. Oh, S. Nakatsuji, Y. Maeno, I. Nagai, S. I. Ikeda, G. Cao, and T. W. Noh, Phys. Rev. B **74**, 113104 (2006).
[24] H. J. Park, C. H. Sohn, D. W. Jeong, G. Cao, K. W. Kim, S. J. Moon, H. Jin, D.-Y. Cho, and T. W. Noh, Phys. Rev. B **89**, 155115 (2014).
[25] C. Liu, S.-Y. Xu, N. Alidoust, T.-R. Chang, H. Lin, C. Dhital, S. Khadka, M. Neupane, I. Belopolski, G. Landolt, H.-T. Jeng, R. Markiewicz, J. H. Dil, A. Bansil, S. D. Wilson, and M. Zahid Hasan, ArXiv e-prints (2014), arXiv:1403.2704 [cond-mat.str-el].
[26] K. Hämäläinen, D. P. Siddons, J. B. Hastings, and L. E. Berman, Phys. Rev. Lett. **67**, 2850 (1991).
[27] H. Gretarsson, J. Kim, D. Casa, T. Gog, K. R. Choi, S. W. Cheong, and Y.-J. Kim, Phys. Rev. B **84**, 125135 (2011).
[28] J. P. Clancy, A. Lupascu, H. Gretarsson, Z. Islam, Y. F. Hu, D. Casa, C. S. Nelson, S. C. LaMarra, G. Cao, and Y.-J. Kim, Phys. Rev. B **89**, 054409 (2014).
[29] S. Boseggia, R. Springell, H. C. Walker, A. T. Boothroyd, D. Prabhakaran, S. P. Collins, and D. F. McMorrow, Journal of Physics: Condensed Matter **24**, 312202 (2012).
[30] K. Ishii, I. Jarrige, M. Yoshida, K. Ikeuchi, J. Mizuki, K. Ohashi, T. Takayama, J. Matsuno, and H. Takagi, Phys. Rev. B **83**, 115121 (2011).
[31] J. Kim, D. Casa, M. H. Upton, T. Gog, Y.-J. Kim, J. F. Mitchell, M. van Veenendaal, M. Daghofer, J. van den Brink, G. Khaliullin, and B. J. Kim, Phys. Rev. Lett. **108**, 177003 (2012).
[32] M. Moretti Sala, K. Ohgushi, A. Al-Zein, Y. Hirata, G. Monaco, and M. Krisch, Phys. Rev. Lett. **112**, 176402 (2014).
[33] W. Schülke, *Electron Dynamics by Inelastic X-Ray Scattering*, Oxford Series on Synchrotron Radiation (OUP Oxford, 2007).
[34] C. Ponchut, J. M. Rigal, J. Clément, E. Papillon, A. Homs, and S. Petitdemange, Journal of Instrumentation **6**, C01069 (2011).
[35] S. Boseggia, R. Springell, H. C. Walker, A. T. Boothroyd, D. Prabhakaran, D. Wermeille, L. Bouchenoire, S. P. Collins, and D. F. McMorrow, Phys. Rev. B **85**, 184432 (2012).
[36] C. T. Chen, F. Sette, Y. Ma, M. S. Hybertsen, E. B. Stechel, W. M. C. Foulkes, M. Schulter, S.-W. Cheong, A. S. Cooper, L. W. Rupp, B. Batlogg, Y. L. Soo, Z. H. Ming, A. Krol, and Y. H. Kao, Phys. Rev. Lett. **66**, 104 (1991).
[37] M. Schmidt, T. R. Cummins, M. Bürk, D. H. Lu, N. Nücker, S. Schuppler, and F. Lichtenberg, Phys. Rev. B **53**, R14761 (1996).
[38] T. Mizokawa, L. H. Tjeng, G. A. Sawatzky, G. Ghiringhelli, O. Tjernberg, N. B. Brookes, H. Fukazawa, S. Nakatsuji, and Y. Maeno, Phys. Rev. Lett. **87**, 077202 (2001).
[39] J. C. Slater and G. F. Koster, Phys. Rev. **94**, 1498 (1954).
[40] M. Subramanian, M. Crawford, and R. Harlow, Materials Research Bulletin **29**, 645 (1994).
[41] W. Harrison, *Electronic structure and the properties of solids: the phys* Dover Books on Physics (Dover Publications, 1989).
[42] I. B. Bersuker, *Electronic Structure and Properties of Transition Metal* (Wiley, 2010).